Phase stabilities of *Cmcm* and *Pnma* SnSe studied by phonon quasiparticle approach

Yong Lu,[1,*] Fa-wei Zheng,[2] Yu Yang,[2] Ping Zhang,[2] and Dong-Bo Zhang[3,4,†]
[1]*Beijing University of Chemical Technology, College of Mathematics and Physics, Beijing 100029, China*
[2]*Institute of Applied Physics and Computational Mathematics, Beijing 100088, China*
[3]*College of Nuclear Science and Technology, Beijing Normal University, Beijing 100875, China*
[4]*Beijing Computational Science Research Center, Beijing 100193, China*

(Received 8 April 2019; revised manuscript received 10 June 2019; published 19 August 2019)

We investigated the structural stability of SnSe from 0 to 800 K by the phonon quasiparticle approach combining first-principles molecular-dynamics (MD) simulations and lattice dynamics. At high temperature, we witness the dynamic stability of the *Cmcm* phase and reveal the coupling of the polarization of phonon modes and the phase transition between the *Cmcm* and *Pnma* phases. Specifically, in real space, the probability distribution of atomic displacements from first-principles MD simulations successfully captures the structural instability at low temperature and the structural stability at high temperature for *Cmcm* SnSe. An analysis of phonon power spectra of several modes also delivers the dynamic stabilization of *Cmcm* at high temperature. Particularly, the soft modes of the Y_1 mode at the $\mathbf{q} = Y(\frac{1}{2}, \frac{1}{2}, 0)$ point and the Γ_1 mode at the $\mathbf{q} = \Gamma(0, 0, 0)$ point of the *Cmcm* phase in the harmonic approximation become relatively rigid at elevated temperature, in agreement with experimental and previous theoretical results. The calculated anharmonic phonon dispersions and density of states are strongly temperature-dependent, and some phonon modes adopt giant frequency shifts. These aspects demonstrate the heavy anharmonicity in SnSe. At low temperature, the transition from the *Cmcm* to the *Pnma* phase induces a symmetry breaking of structure. Consequently, the degeneracy of associated electronic states (mainly p states) is lifted, thus lowering the energy of the *Pnma* phase.

DOI: 10.1103/PhysRevB.100.054304

I. INTRODUCTION

Given the reported high value of the figure of merit [1,2], SnSe has emerged as one of the most promising thermoelectric materials and invited extensive investigations. At low temperature, SnSe adopts a *Pnma* symmetry. At high temperature, a phase transition toward a *Cmcm* phase is possible via a second-order displacive procedure [3–5]. What is interesting is that the figure of merit of the *Cmcm* phase is much larger than that of the *Pnma* phase [1]. Efforts were also devoted to improving the thermoelectric performance of SnSe by considering polycrystalline SnSe [6–9], n-type doping [10,11], pressure [12], p-type doping [13–16], and out-of-plane transport of charge [17].

The excellent thermoelectric performance of SnSe is closely related to its lattice anharmonicity. For example, a recent experiment [18] revealed that phonons in SnSe display giant anharmonicity, associated with a soft-mode lattice instability driven by the resonantly bonding Se p states and chemically inert Sn lone pairs. The highly anharmonic bonding leads to very strong phonon-phonon scattering and anisotropic crystal structure. On the theoretical side, Skelton *et al.* [19] also showed that *Cmcm* SnSe is of strong lattice anharmonicity and the soft modes have a pronounced effect on reducing the lattice thermal conductivity. The *Pnma* phase also displays strong anharmonicity. For example, by measuring the elastic properties of *Pnma* phase SnSe, Xiao *et al.* [20] showed that the weak chemical bonding in SnSe generally causes phonon mode softening, which eventually slows down phonon propagation and thus leads to low lattice thermal conductivity. Combing experiments and first-principles calculations, Bansal *et al.* [21] also revealed strong lattice anharmonicity in *Pnma* SnSe.

However, in spite of the intensive studies on the phonon anharmonicity of SnSe, the discussion on the coupling of electronic structure with phase stability is less concerned [17]. In this work, we investigate the phonon and electronic properties of SnSe with first-principles calculations. To fully capture the anharmonic effect, we employ a phonon quasiparticle approach that depicts phonon quasiparticles numerically [22–24]. With it, we verify the dynamic stability of *Cmcm* SnSe at high temperature and elucidate the coupling of polarization of phonon modes and the second-order phase transition. On the other hand, in the low-temperature domain, we analyze the electronic structures of both phases. For the transition from the *Cmcm* to the *Pnma* phase, the structural symmetry breaking lifts the degeneracy of electronic states, resulting in the energetic stability of the *Pnma* phase.

II. METHODS AND COMPUTATIONAL DETAILS

A phonon quasiparticle can be numerically depicted with the autocorrelation function (VAF) of mode-projected

---

[*] Corresponding author: luy@mail.buct.edu.cn
[†] dbzhang@bnu.edu.cn

2469-9950/2019/100(5)/054304(7)

velocity [22],

$$\langle \mathbf{V}(0)\cdot\mathbf{V}(t)\rangle_{\mathbf{q},s} = \lim_{t_0\to\infty}\frac{1}{t_0}\int_0^{t_0}\mathbf{V}_{\mathbf{q},s}(t')\mathbf{V}_{\mathbf{q},s}(t'+t)dt', \quad (1)$$

and the mode-projected velocity of normal mode $(\mathbf{q}, s)$ is

$$\mathbf{V}_{\mathbf{q},s}(t) = \sum_{i=1}^{N}\mathbf{V}(t)e^{-i\mathbf{q}\cdot\mathbf{R}_i}\cdot\hat{e}_{\mathbf{q},s}, \quad (2)$$

where $\mathbf{V}(t) = \{v_1(t)\sqrt{M_1},\ldots,v_N(t)\sqrt{M_N}\}$ with $3N$ components is the mass weighted velocity, and $v_i(t)$ $(i = 1,\ldots,N)$ are atomic velocities obtained from first-principles MD with N atoms per supercell. $\hat{e}_{\mathbf{q},s}$ is the polarization vector of the harmonic phonon of mode $(\mathbf{q}, s)$, which can be routinely obtained by performing phonon calculations with the standard DFPT approach [25,26]. M_i and $\mathbf{R}_i$ are the atomic mass and coordinates of atom i in the supercell. For a well-defined phonon quasiparticle, VAF decays in an oscillatory way, and its Fourier transform, i.e., the power spectrum $G_{\mathbf{q},s}(\omega)$,

$$G_{\mathbf{q},s}(\omega) = \int_0^{\infty}\langle \mathbf{V}(0)\cdot\mathbf{V}(t)\rangle_{\mathbf{q},s}e^{i\omega t}dt, \quad (3)$$

follows a Lorentzian-type line shape, where both the renormalized phonon frequency $\tilde{\omega}_{\mathbf{q},s}$ and linewidth $\Gamma_{\mathbf{q},s}$ can be extracted from $G_{\mathbf{q},s}$.

The first-principles MD simulations were carried out using density functional theory with the projected-augmented-wave (PAW) method [27] as implemented in the VASP package [28]. The electron exchange and correlation potential is described by the generalized gradient approximation (GGA) parametrized by Perdew-Burke-Ernzerhof revised for solids (PBEsol) [29,30]. The plane-wave cutoff is set to 500 eV, and Fermi-Dirac smearing corresponding to the simulation temperature is adopted. The $4\times2\times4$ supercells containing 256 atoms were used for both *Cmcm* and *Pnma* SnSe. A $2\times1\times2$ k-point grid with the Monkhorst-Pack scheme was used for the Brillouin zone integration [31]. Simulations were carried out at temperatures from 0 to 800 K, and a 1 fs time step was adopted. The relaxed volumes of 204.39 Å^3 with lattice parameters of $a = 4.214$ Å, $b = 11.531$ Å, and $c = 4.206$ Å for the *Cmcm* phase and 206.48 Å^3 with $a = 4.369$ Å, $b = 11.396$ Å, and $c = 4.147$ Å for the *Pnma* phase were employed. To take into account the volumetric thermal expansion, the experimental volume of 217.34 Å^3 with $a = 4.310$ Å, $b = 11.705$ Å, and $c = 4.318$ Å [32] was also considered in the MD simulations at 800 K. To minimize statistical error, a long MD simulation time of 80 ps was used for each temperature. The harmonic force constants were calculated using the DFPT approach in VASP [25,26], and then the harmonic phonon dispersions and polarization vectors were obtained by the postprocessing package PHONOPY [33]. The renormalized phonon-dispersion relations were obtained using a uniform $4\times2\times4$ $\mathbf{q}$ mesh. For self-consistent electronic structure calculations, the $12\times9\times12$ k-point mesh was used for the Brillouin zone integration of the primitive cell.

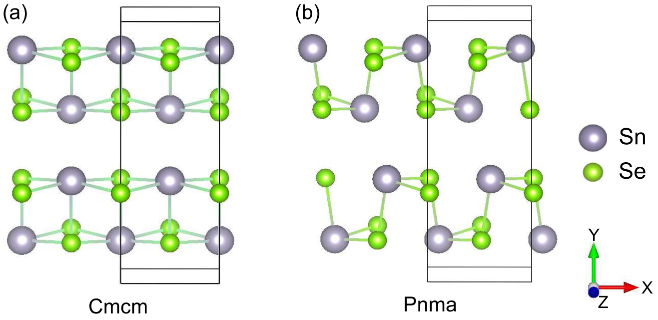

FIG. 1. The crystal structure of SnSe in the *Cmcm* (a) and *Pnma* (b) phases. The same crystal axes are chosen to facilitate the comparison between the *Cmcm* and *Pnma* phases.

III. RESULTS AND DISCUSSIONS

A. Dynamic instability

The crystal structure of SnSe for the high-temperature base-centered orthorhombic *Cmcm* phase and the room-temperature orthorhombic *Pnma* phase are illustrated in Figs. 1(a) and 1(b), respectively. The same crystal axes are chosen to facilitate the comparison between these two phases. The symmetry of the *Cmcm* phase is higher than that of the *Pnma* phase, mainly because of the distortion of Sn atoms along the x direction in the *Pnma* phase. The harmonic phonon dispersion of the *Cmcm* phase at a volume of 204.39 Å^3 was calculated using the DFPT approach, as shown in Fig. 2(a). Clearly, the imaginary phonon frequencies of modes along the Γ-Y path hint at the phase instability of the *Cmcm* phase at low temperature. From an analysis of the phonon eigenvectors, at the Γ point, the soft mode is ferroelectric-like with all Sn atoms moving toward $+z$ while all Se atoms move toward $-z$ [34]. For the soft TA mode of $\mathbf{q} = Y(\frac{1}{2},\frac{1}{2},0)$ (labeled as Y_1), Sn atoms in the lower

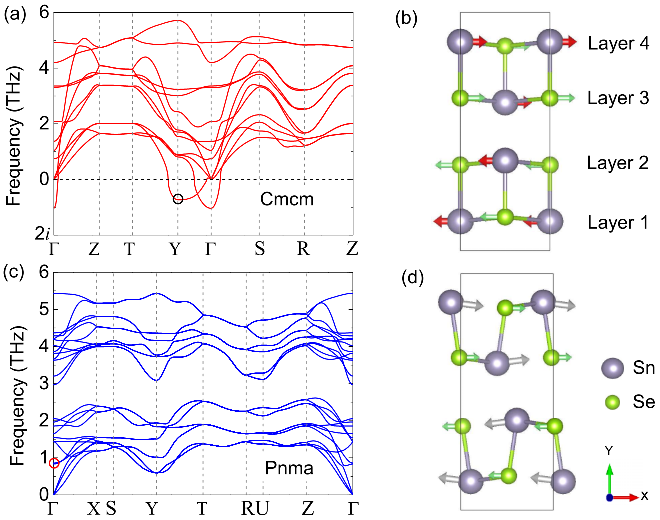

FIG. 2. The calculated phonon-dispersion curves of (a) the *Cmcm* phase along Γ-Z-T-Y-Γ-S-R-Z and (c) the *Pnma* phase along Γ-X-S-Y-T-R-U-Z-Γ at 0 K. Parts (b) and (d) show the phonon eigenvectors of the Y_1 mode as marked by a black circle in (a) for the *Cmcm* phase and the lowest transverse optical (TO$_c$) mode as marked by a red circle in (b) for the *Pnma* phase, respectively.

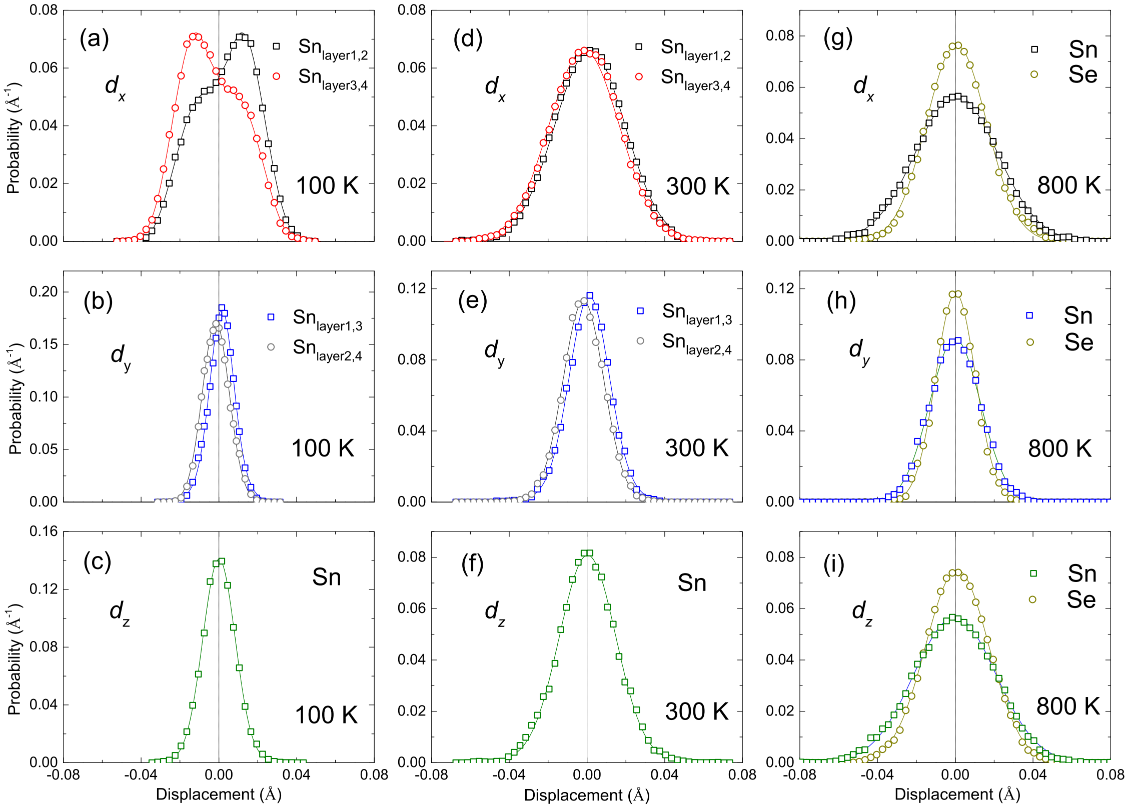

FIG. 3. Probability distributions of atomic displacements along (a) x, (b) y, and (c) z directions with respect to the ideal *Cmcm* structure for Sn atoms at 100 K. (d)–(f) The same as (a)–(c) but at 300 K. (g)–(i) The same as (a)–(c) but for both Sn and Se atoms at 800 K. The square and circle symbols stands for the data from first-principles MD simulations, and the solid lines are the fitting results.

bilayer (layers 1 and 2) and the upper bilayer (layers 3 and 4) move along the $-x$ and $+x$ directions, respectively, as shown in Fig. 2(b), corresponding to symmetry-breaking displacive distortions. For the low-temperature *Pnma* phase, the phonon dispersion curves are stable throughout the Brillouin zone, Fig. 2(c). For the temperature-driven phase transition from *Cmcm* to *Pnma*, the Y point of the *Cmcm* phase becomes the Γ point in the *Pnma* phase, where the soft Y_1 mode is now the lowest transverse optical (TO$_c$) mode in *Pnma* [Fig. 2(d)], consistent with experimental observations [18].

The first-principles MD simulations were performed to elucidate the structural stability of the *Cmcm* phase with temperature. Figure 3 shows the probability distribution of atomic displacements along different directions for Sn and Se atoms. At 100 K, the Sn atoms show two splitting distribution peaks in the x direction, as shown in Fig. 3(a). Because the distribution function has two maxima at the nonzero displacements, the *Cmcm* structure at 100 K is not stable. In detail, Sn atoms in layers 1 and 2 (layers 3 and 4) tend to move for 0.016 (-0.016) Å along the $+x$ ($-x$) direction. The double-peak shape of the probability distribution is also found in the y direction with smaller deviation. In this way, due to thermal fluctuations, Sn atoms actually prefer to stay at the Wyckoff 4c site of the *Pnma* structure. This explains the displacive phase transition.

As temperature increases, thermal fluctuations cause the discrete peaks in the *Pnma* probability distribution function to merge. For example, at 800 K, the probability distribution displays only one peak with the maximum at the zero displacement with respect to the ideal *Cmcm* structure. Due to symmetry, the atomic distribution curves along the x and z directions are identical, and all three coordination directions show a Gaussian function distribution for both Sn and Se atoms, as shown in Figs. 3(g)–3(i). Thus, we conclude that the *Cmcm* lattice is now stable.

B. Anharmonic phonon dispersion relations

Dynamic stability can also be inferred from an analysis of the velocity autocorrelation function (VAF), i.e., phonon quasiparticles. Figure 4(a) shows the VAFs of the typical Y_1 and Y_3 modes at 800 K, which both display oscillatory decaying behaviors, a sign of structural stability. The associated power spectra shown in Fig. 4(b) are of well-defined Lorentzian line shape with a single peak. It allows us to identify the phonon frequency and linewidth of these modes: $\tilde{\omega}_{\mathbf{q},s} = 0.44$ THz and $\Gamma_{\mathbf{q},s} = 0.35$ THz for the Y_1 mode and $\tilde{\omega}_{\mathbf{q},s} = 0.84$ THz and $\Gamma_{\mathbf{q},s} = 0.44$ THz for the Y_3 mode. It is worth noting that the Y_1 mode has a harmonic frequency of 0.78i THz. Thus, one can see that the Y_1 mode has a huge frequency shift of 1.22 THz. On contrast, for the Y_3 mode whose harmonic frequency is 0.84 THz, the frequency shift is much smaller. At a volume of 204.39 Å^3, the frequency shifts are 1.35 and 0.12 THz for the Y_1 and Y_3 modes, respectively.

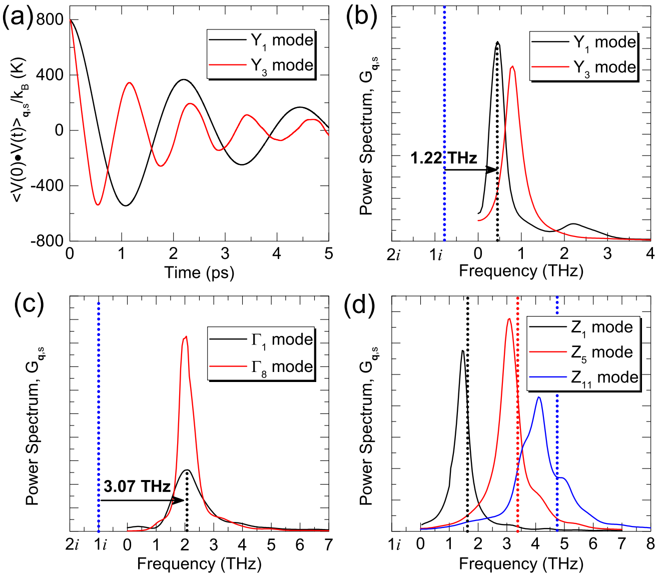

FIG. 4. (a) The velocity autocorrelation function (VAF), $\langle \mathbf{V}(0)\cdot\mathbf{V}(t)\rangle_{\mathbf{q},s}$, of the Y_1 and Y_3 modes at $\mathbf{q} = Y(\frac{1}{2}, \frac{1}{2}, 0)$ for the *Cmcm* phase. (b) The power spectrum, $G_{\mathbf{q},s}$, of the Y_1 and Y_3 modes. The dotted blue line indicates the harmonic frequency of 0.78*i* THz for the Y_1 mode. (c) The power spectrum of the Γ_1 and Γ_8 modes at the $\mathbf{q} = \Gamma(0, 0, 0)$ point of the *Cmcm* phase. The dotted blue line represents the harmonic frequency of 1.00*i* THz for the Γ_1 mode. (d) The power spectrum of Z_1, Z_5, and Z_{11} modes at the $\mathbf{q} = Z(\frac{1}{2}, \frac{1}{2}, \frac{1}{2})$ point. The dotted black, red, and blue lines represent the corresponding harmonic frequencies of 1.64, 3.38, and 4.75 THz, respectively. The calculation temperature is 800 K.

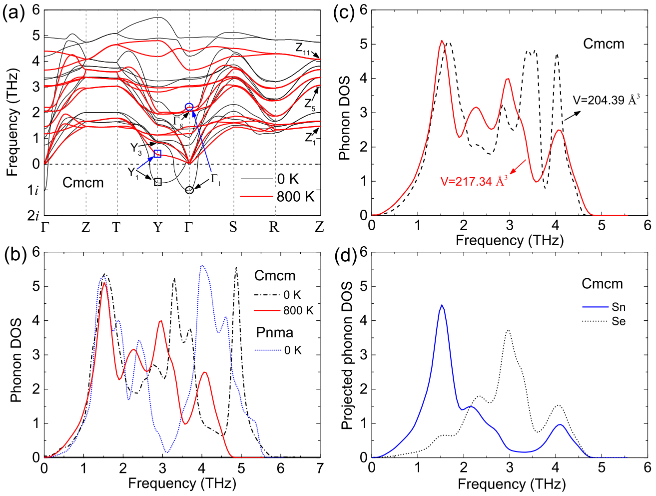

FIG. 5. (a) The calculated anharmonic phonon dispersions of the *Cmcm* phase SnSe based on the phonon quasiparticle approach at 800 K (solid red curves). The experimental volume of 217.34 Å^3 was used. The harmonic results calculated by DFPT at 0 K (solid black curves) are shown for comparison. The phonon modes displayed in Fig. 4 are marked. (b) The phonon density of states (DOS) of *Cmcm* SnSe at 800 K is shown by a solid red line. For comparison, the harmonic results calculated by DFPT for the *Cmcm* (dash-dotted curve) and *Pnma* (dotted curve) phases are also shown. (c) The comparison of anharmonic phonon DOS calculated at volumes of 217.34 and 204.39 Å^3 from the phonon quasiparticle approach, respectively. (d) The decomposition of anharmonic phonon DOS with respect to Sn and Se atoms at a volume of 217.34 Å^3.

We note that the very anharmonic Y_1 mode is closely related to the lowest TO$_c$ mode of the *Pnma* phase, which also displays strong anharmonicity. Indeed, the inelastic neutron scattering (INS) experiments have shown that the temperature strongly affects the lowest TO$_c$ mode at the Γ point of the *Pnma* phase [18]. When the *Pnma* phase transits to the *Cmcm* phase, the lowest TO$_c$ mode of *Pnma* becomes the Y_1 mode, which can be verified by the phonon eigenvector in Figs. 2(b) and 2(d). The calculated anharmonic frequency of 0.44 THz for Y_1 is in agreement with ~0.48 THz of the TO$_c$ mode obtained by experiment at 800 K [18].

The power spectrum of Γ_1 and Γ_8 modes also obeys the Lorentzian line shape, as shown in Fig. 4(c). The giant frequency shift is also found for the Γ_1 mode. This mode has a harmonic frequency of 1.00*i* THz and an anharmonic frequency of 2.07 THz at 800 K. For the Γ_8 mode with a harmonic frequency of 2.02 THz, the frequency shift is relatively small. The Lorentzian line shape of the power spectra for individual modes validates the phonon picture. For a systematic check, we have inspected all the sampled phonon modes. Figure 4(d) shows the power spectra of three phonon modes at the $\mathbf{q} = Z(\frac{1}{2}, \frac{1}{2}, \frac{1}{2})$ point, i.e., Z_1, Z_5, and Z_{11}, covering from the low-frequency to the high-frequency domain. All these modes display the typical Lorentzian-type line shape with a single peak, indicating the validity of the concept of phonon quasiparticles for these modes.

With the renormalized phonon frequencies $\widetilde{\omega}_{\mathbf{q},s}$ extracted from all the $\mathbf{q}$ points sampled in first-principles MD simulations, our approach is able to calculate the anharmonic phonon dispersions over the whole Brillouin zone [22,35]. Figure 5(a) shows the phonon spectra of *Cmcm* SnSe at 800 K along the same path as that in Fig. 2(a). The experimental volume of 217.34 Å^3 is used here. Considering the anharmonic interaction, the high-temperature phonon-dispersion curves become stable, where the imaginary frequencies presented in the DFPT calculation vanish.

The phonon modes displayed in Fig. 4 are marked in Fig. 5(a), from which we can also see the huge temperature-induced frequency shift for these modes. Four typical peaks can be clearly seen from the phonon density of states as shown in Fig. 5(b). At 800 K, the four peaks are located at 1.5 THz (peak-1), 2.3 THz (peak-2), 2.9 THz (peak-3), and 4.1 THz (peak-4), respectively. Compared with the DFPT data at 0 K, all four peaks are shifted toward the low-frequency level. The effect of volume expansion is mainly on the medium-frequency region, which can be observed by comparing the phonon DOS at volumes of 217.34 and 204.39 Å^3, Fig. 5(c). Peak-2 and peak-3 shift to the low-frequency region by 0.5 and 0.6 THz, respectively, when considering volume expansion. From the decomposition of the phonon density of states with respect to Sn and Se atoms in Fig. 5(d), it is found that the low-frequency peak-1 is mainly contributed by Sn vibrations while peak-3 is dominated by Se atoms. Peak-2 and peak-4 originate from the coupling of Sn and Se displacements. When transitioning to the *Pnma* phase, the four successive peaks are separated into two parts between peak-2 and peak-3, while

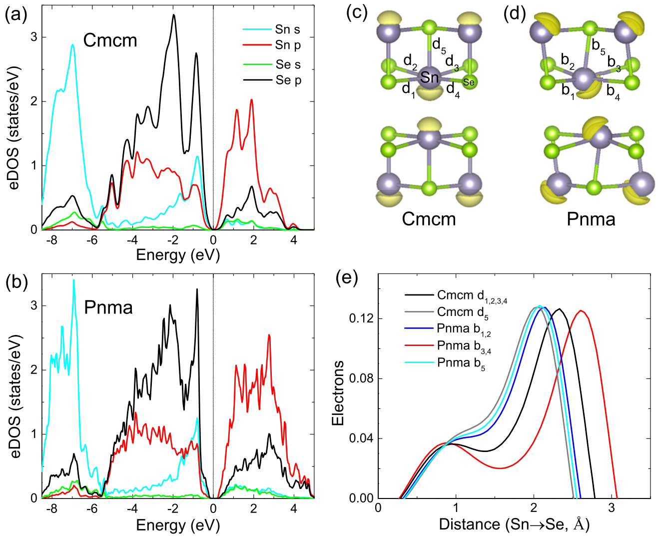

FIG. 6. The calculated electronic density of states of (a) the *Cmcm* phase at 204.39 Å^3 and (b) the *Pnma* phase. The valence electron density (isosurface at 0.04 $e/\text{Å}^3$) for (c) the *Cmcm* phase and (d) the *Pnma* phase. (e) The linear distribution of electronic density along different bonding directions for the *Cmcm* and *Pnma* phases. Parts (c)–(e) were drawn with the help of VESTA software [36].

peak-4 is merged into peak-3. The free energy contributed by the lattice vibrations is -120.71 kJ/mol at 800 K for the *Cmcm* phase, reduced by 96.21 kJ/mol with respect to the *Pnma* phase at 300 K.

C. Electronic structure

The calculated orbital-projected electronic density of states of the *Cmcm* phase shows that bonding states near the Fermi level are dominated by Se *p* states hybridized with Sn *s* and *p* states, as shown in Fig. 6(a). Three sharp peaks from the Se *p* orbital and Sn *s*, *p* orbitals right below the valence-band maximum (VBM) indicate that these orbitals contribute greatly to the chemical bonding. For the *Pnma* SnSe, the Sn *s* peak is broadened slightly with respect to the *Cmcm* phase, Fig. 6(b). The electronic temperature was applied by the Fermi-Dirac smearing with a given width. For the low-temperature *Pnma* phase, the band gap is 0.40 eV with a width of 0.026 eV, Fig. 6(b). When there is a transition to the *Cmcm* phase at 800 K, the band gap decreases to 0.05 eV with a width of 0.069 eV, Fig. 6(a). For the orbital-projected band structures, the band degeneracy in the *Cmcm* phase is higher than that in the *Pnma* phase, Fig. 7. The p_x, p_y, and p_z orbitals of the Se atom in the *Cmcm* phase are all occupied with an equal amount of electrons (0.75 per atom). For the *Pnma* phase, these three orbitals are occupied by 0.78, 0.76, and 0.77 electrons per atom, respectively. The structural distortion induces a lifting of the degeneracy of states, which lowers the energy of *Pnma* SnSe according to the known Jahn-Teller effect. The reduced band gap and increased band degeneracy in the high-temperature *Cmcm* phase are both in support of the electronic contribution to the thermoelectric performance of SnSe.

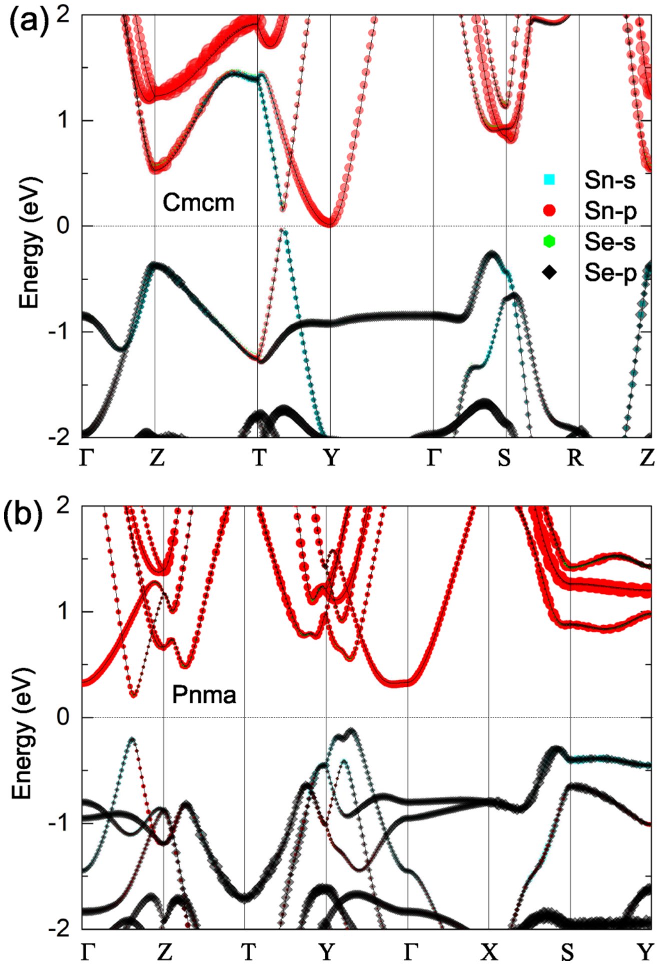

FIG. 7. The orbital-projected band structures of (a) the *Cmcm* phase along the high-symmetry Γ-*Z*-*T*-*Y*-Γ-*S*-*R*-*Z* path and (b) the *Pnma* phase along the Γ-*Z*-*T*-*Y*-Γ-*X*-*S*-*Y* path in the Brillouin zone, respectively. The thickness of the curves hints at the degree of the state degeneracy.

Since the *Cmcm* phase has a higher symmetry than the *Pnma* phase, the phase transition from *Cmcm* to *Pnma* gives rise to symmetry breaking of associated electronic states. In the *Cmcm* phase, the four Sn-Se bonds (d_1–d_4) are identical, Fig. 6(c), forming the resonant bonds. For the phase transition from *Cmcm* to *Pnma*, Sn atoms move along the *x* and *y* directions, causing a symmetry breaking. As a result, the degeneracy between Sn-Se bonds is lifted with two shorter (stronger) bonds ($b_{1,2}$) and two longer (weaker) bonds ($b_{3,4}$), as shown in Fig. 6(d). Only the d_5 bond along the *y* direction is nearly unaffected. The distributions of electron density along different bonding directions as shown in Fig. 6(e) present the differences of Sn-Se bonds quantitatively. The locations of the distribution peaks for the $b_{1,2}$ and $b_{3,4}$ bonds in the *Pnma* phase deviate clearly from the positions of the d_1–d_4 bonds in the *Cmcm* phase. As a result, the Bader effective charges are $+1.40$ for Sn and -1.40 for Se in the *Cmcm* phase, and $+2.12$ for Sn and -2.12 for Se in the *Pnma* phase. The ionicity in the *Pnma* phase is more obvious. From the electronic density distribution, an isolated lobe around each Sn atom formed by stereochemically active lone pairs is depicted in

Figs. 6(c) and 6(d). For the high-symmetry bonds in the *Cmcm* phase, the lone pairs point opposite the d_5 bond along the y axis toward the interlayer. In the *Pnma* phase, due to the coupling with the nearest-neighbor Se atoms, the lone pairs deviate from the y axis, inclined to the opposite direction of $b_{1,2}$ bonds, in agreement with Ref. [18]. Compared to the *Cmcm* phase, the stronger ionicity and deviation of lone pairs from the y axis in the *Pnma* phase weaken the electronic transport in the intra- and interlayer directions to a certain extent.

IV. DISCUSSIONS AND SUMMARY

The phase transition between *Cmcm* and *Pnma* SnSe is a second-order displacive transition. At high temperature, the *Cmcm* phase is more favorable mainly due to the thermal fluctuations. Our simulations with the phonon quasiparticle approach verify this. In particular, the soft Y_1 and Γ_1 modes in the harmonic approximation become relatively rigid when the anharmonic effect is accounted for at high temperature. Moreover, both Y_1 and Γ_1 modes adopt giant phonon frequency shifts with temperature. These facts reveal the strong anharmonicity in SnSe. At low temperature, the *Pnma* phase is more stable. We attribute this to a stabilization according to the Jahn-Teller effect. Namely, the symmetry breaking of the structure causes a lift of state degeneracy, bringing a lowering of energy of SnSe. For the transition from the *Pnma* to the *Cmcm* phase, the coupling of increased phonon anharmonicity and band degeneracy, and the reduced band gap and ionicity, enables SnSe to have a superior thermoelectric performance.

ACKNOWLEDGMENT

This work is supported by the National Natural Science Foundation of China under Grants No. 11704020 and No. 11874088.

---

[1] L.-D. Zhao, S. H. Lo, Y. S. Zhang, H. Sun, G. J. Tan, C. Uher, C. Wolverton, V. P. Dravid, and M. G. Kanatzidis, Nature (London) **508**, 373 (2014).

[2] L.-D. Zhao, G. J. Tan, S. Q. Hao, J. Q. He, Y. L. Pei, H. Chi, H. Wang, S. K. Gong, H. B. Xu, V. P. Dravid, C. Uher, G. J. Snyder, C. Wolverton, and M. G. Kanatzidis, Science **351**, 141 (2016).

[3] T. Chattopadhyay, J. Pannetier, and H. G. Vonschnering, J. Phys. Chem. Solids **47**, 879 (1986).

[4] W. J. Baumgardner, J. J. Choi, Y.-F. Lim, and T. Hanrath, J. Am. Chem. Soc. **132**, 9519 (2010).

[5] U. Aseginolaza, R. Bianco, L. Monacelli, L. Paulatto, M. Calandra, F. Mauri, A. Bergara, and I. Errea, Phys. Rev. Lett. **122**, 075901 (2019).

[6] S. Sassi, C. Candolfi, J.-B. Vaney, V. Ohorodniichuk, P. Masschelein, A. Dauscher, and B. Lenoir, Appl. Phys. Lett. **104**, 212105 (2014).

[7] S. Sassi, C. Candolfi, J.-B. Vaney, V. Ohorodniichuk, P. Masschelein, A. Dauscher, and B. Lenoir, Mater. Today: Proc. **2**, 690 (2015).

[8] T. R. Wei, C.-F. Wu, X. Z. Zhang, Q. Tan, L. Sun, Y. Pan, and J.-F. Li, Phys. Chem. Chem. Phys. **17**, 30102 (2015).

[9] Y. X. Chen, Z. H. Ge, M. J. Yin, D. Feng, X. Q. Huang, W. Y. Zhao, and J. Q. He, Adv. Funct. Mater. **26**, 6836 (2016).

[10] R. Q. Guo, X. J. Wang, Y. D. Kuang, and B. L. Huang, Phys. Rev. B **92**, 115202 (2015).

[11] Y. Suzuki and H. Nakamura, Phys. Chem. Chem. Phys. **17**, 29647 (2015).

[12] I. Loa, R. J. Husband, R. A. Downie, S. R. Popuri, and J-W. G. Bos, J. Phys.: Condens. Matter **27**, 072202 (2015).

[13] N. K. Singh, S. Bathula, B. Gahtori, K. Tyagi, D. Haranath, and A. Dhar, J. Alloys Compd. **668**, 152 (2016).

[14] M. Gharsallah, F. Serrano-Sánchez, N. M. Nemes, F. J. Mompeán, J. L. Martnez, M. T. Fernández-Díaz, F. Elhalouani, and J. A. Alonso, Sci. Rep. **6**, 26774 (2016).

[15] Z. H. Ge, D. S. Song, X. Y. Chong, F. S. Zheng, L. Jin, X. Qian, L. Zheng, R. E. Dunin-Borkowski, P. Qin, J. Feng, and L.-D. Zhao, J. Am. Chem. Soc. **139**, 9714 (2017).

[16] Q. S. Lu, M. H. Wu, D. Wu, C. Chang, Y. P. Guo, C. S. Zhou, W. Li, X. M. Ma, G. Wang, L.-D. Zhao, L. Huang, C. Liu, and J. Q. He, Phys. Rev. Lett. **119**, 116401 (2017).

[17] C. Chang, M. Wu, D. He, Y. Pei, C.-F. Wu, X. Wu, H. Yu, F. Zhu, K. Wang, Y. Chen, L. Huang, J.-F. Li, J. He and L.-D. Zhao, Science **360**, 778 (2018).

[18] C. W. Li, J. Hong, A. F. May, D. Bansal, S. Chi, T. Hong, G. Ehlers, and O. Delaire, Nat. Phys. **11**, 1063 (2015).

[19] J. M. Skelton, L. A. Burton, S. C. Parker, A. Walsh, C. E. Kim, A. Soon, J. Buckeridge, A. A. Sokol, C. R. A. Catlow, A. Togo, and I. Tanaka, Phys. Rev. Lett. **117**, 075502 (2016).

[20] Y. Xiao, C. Chang, Y. Pei, D. Wu, K. Peng, X. Zhou, S. Gong, J. He, Y. Zhang, Z. Zeng, and L.-D. Zha, Phys. Rev. B **94**, 125203 (2016).

[21] D. Bansal, J. W. Hong, C. W. Li, A. F. May, W. Porter, M. Y. Hu, D. L. Abernathy, and O. Delaire, Phys. Rev. B **94**, 054307 (2016).

[22] D.-B. Zhang, T. Sun, and R. M. Wentzcovitch, Phys. Rev. Lett. **112**, 058501 (2014).

[23] T. Sun, D.-B. Zhang, and R. M. Wentzcovitch, Phys. Rev. B **89**, 094109 (2014).

[24] Y. Lu, T. Sun, and D.-B. Zhang, Phys. Rev. B **97**, 174304 (2018).

[25] S. Baroni, P. Giannozzi, and A. Testa, Phys. Rev. Lett. **58**, 1861 (1987).

[26] S. Baroni, S. de Gironcoli, and A. Dal Corso, Rev. Mod. Phys. **73**, 515 (2001).

[27] P. E. Blöchl, Phys. Rev. B **50**, 17953 (1994).

[28] G. Kresse and J. Furthmöller, Phys. Rev. B **54**, 11169 (1996).

[29] J. P. Perdew, K. Burke, and M. Ernzerhof, Phys. Rev. Lett. **77**, 3865 (1996).

[30] J. P. Perdew, A. Ruzsinszky, G. I. Csonka, O. A. Vydrov, G. E. Scuseria, L. A. Constantin, X. Zhou, and K. Burke, Phys. Rev. Lett. **100**, 136406 (2008).

[31] H. J. Monkhorst and J. D. Pack, Phys. Rev. B **13**, 5188 (1976).

[32] H. G. Schnering and H. Wiedemeier, Z. Krist.-Cryst. Mater. **156**, 143 (1981).

[33] A. Togo, L. Chaput, I. Tanaka, and G. Hug, Phys. Rev. B **81**, 174301 (2010).

[34] C. Stock, P. M. Gehring, R. A. Ewings, G. Xu, J. Li, D. Viehland, and H. Luo, Phys. Rev. Mater. **2**, 024404 (2018).

[35] Y. Lu, T. Sun, P. Zhang, P. Zhang, D.-B. Zhang, and R. M. Wentzcovitch, Phys. Rev. Lett. **118**, 145702 (2017).

[36] K. Momma and F. Izumi, J. Appl. Crystallogr. **44**, 1272 (2011).